Materials Science and Engineering B 290 (2023) 116296

Contents lists available at ScienceDirect

Materials Science & Engineering B

journal homepage: www.elsevier.com/locate/mseb

Effect of La and Se in tailoring the energy storage properties of BFO nanostructures

A. Joana Preethi [a,*], T. Sharmili [a], J. Vigneshwaran [b], Sujin P. Jose [b], M. Ragam [a]

[a] Research Centre of Physics, Fatima College (Autonomous), Affiliated to Madurai Kamaraj University, Madurai, Tamil Nadu, India
[b] School of physics, Madurai Kamaraj University, Madurai, India

ARTICLE INFO

Keywords:
BFO
Solvothermal
Dielectric
Magnetic
Supercapacitor

ABSTRACT

Simultaneous rare-earth doping at A and B sites have impacted various properties of BFO at room temperature. In this work, the dielectric and magnetic properties of BFO, are tailored by doping La and Se. $Bi_{0.92}La_{0.08}Fe_{1-x}Se_xO_3$, (x = 0%, 10%, 25%, 50%, 100%) nanostructures are prepared using sol-gel technique. Structural analysis reveals that increased doping has reduced and eliminated the secondary phases of nanostructures. Absorption spectra showed a wide blue shifted absorption, indicating multiple electron transitions and the bandgap values decreased upon doping. Improved room temperature dielectric properties with increased doping indicates these nanostructures as viable candidates in energy storage applications. The improvements in ac-conductivity, impedance and modulus spectrum of doped nanostructures are observed. Specific capacitance of 36.22 F/g for $Bi_{0.92}La_{0.08}Fe_1O_3$ at 10 mV/s and 21.48F/g for the $Bi_{0.92}La_{0.08}Fe_{0.9}Se_{0.1}O_3$ sample was observed. Weak ferromagnetism is observed in M-H loops with increased Se concentration that also finds applications in magnetic storage devices.

1. Introduction

Multiferroics are an interesting class of multifunctional materials that have attracted considerable attention because they exhibit multiple ferroic orders, such as ferroelectricity, ferromagnetism, and ferroelasticity. The coupling of electric and magnetic properties has been found to be useful in various applications including energy storage, data storage, ferroelectric field-effect transistors (FeFETs), sensors, actuators, and spintronics [1,2]. Bismuth Ferrite (BFO) has recently been one of the most researched topics owing to its room temperature multiferroic properties that makes it a potential candidate for applications in numerous fields including smart devices, memory devices, sensors and energy storage applications.

In the later years, researchers have focused their efforts on developing electrochemical devices for energy conversion and energy storage to address issues such as depletion of fossil fuel supplies, increasing energy cost and environmental pollution [3]. Very recently, works were reported on the synthesis of high performance electrode materials with appreciable cycle period [4–6]. In terms of power and energy density, supercapacitors are seen to be a viable alternative to Lithium-ion batteries because of their high power density and long service life. The supercapacitors bridge the gap between normal capacitors and batteries [7]. Supercapacitors are categorized by charge storage techniques. Electric double layer capacitors (EDLcs) have high power density and a long cycle life while pseudocapacitors have high energy density and high specific capacitance. But, their applicability is limited by weak conductivity and low active material usage rates [8]. Recently, Dielectric materials with high energy storage density, good temperature stability, and low dielectric loss have gained potential applications in capacitor technology. Developing capacitors with improved energy density, storage efficiency and operation sustainability in severe environments are one of the main aim of the ceramic industry.

To enhance the features of present electrochemical energy storage devices, the dielectric properties and magnetic properties of nanostructures need to be optimized and finding a suitable dielectric material is vital for industrial applications. The ferroelectric and ferromagnetic properties of BFO multiferroics can be tuned by the substitution of A-site cation with rare earth elements or by replacing the B-site cation with transition metals and rare earth elements [9]. In this context, various attempts have been made by doping the A and B sites of BFO nanostructures with Rare earth elements such as lanthanum (La) and selenium (Se) to enhance the optical and dielectric properties that may

* Corresponding author.
E-mail address: jonapreethi08@gmail.com (A. Joana Preethi).

https://doi.org/10.1016/j.mseb.2023.116296
Received 8 July 2022; Received in revised form 5 January 2023; Accepted 17 January 2023
Available online 27 January 2023

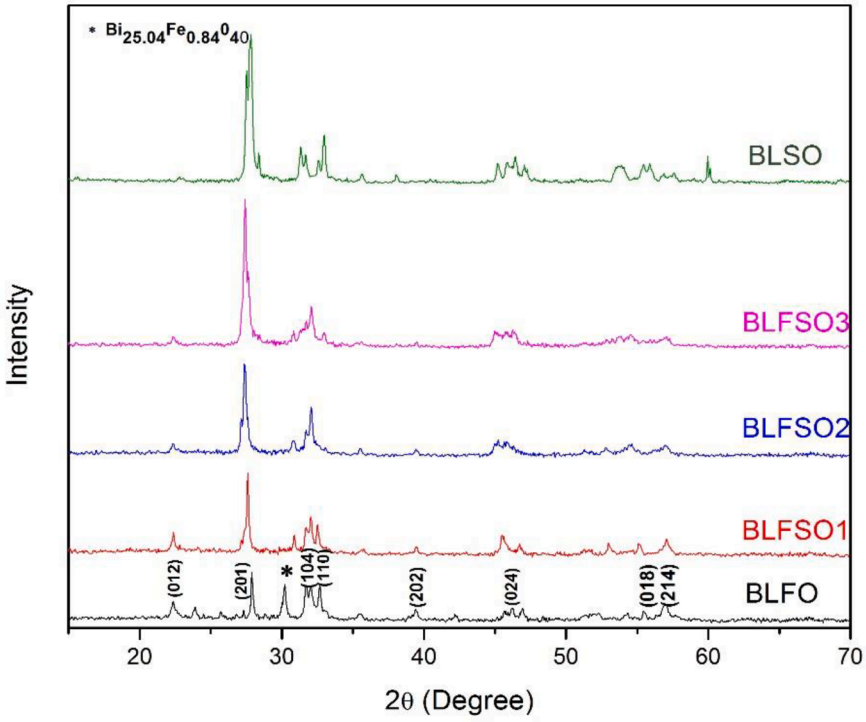

Fig. 1. XRD patterns of La, Se doped BFO nanostructures.

impact the conductivity properties toward energy production and energy storage applications. It is reported that the A-site substitution improves the magnetization and dielectric properties and the B-site doping reported enhanced magnetic properties, making them suitable candidates for supercapacitor applications [10]. Also, much progress has been achieved on the rare earth-doped Perovskite oxide nanostructures after considerable experimental and theoretical efforts. The unique magnetic, electrical and spectroscopic properties of rare-earth elements were reported to improve the efficiency of energy conversion processes. It is believed that smaller A-site cations (La) and vacancies introduced in the lattice due to rare earth doping tend to cause a chemical pressure, leading to tilting and compression of oxygen octahedrons in the antiferroelectric distortive configuration of BFO. Thus, affecting the electrical and magnetic properties of the material. Hence, such dopants are opted to enhance the multiferroic properties of the material, aiding its energy conversion and energy storage properties.

2. Experimental technique

Various samples of (La, Se) co-doped BFO nanoparticles with empirical formula $Bi_{0.92}La_{0.08}Fe_{1-x}Se_xO_3$, (x = 0%, 10%, 25%, 50%, 100%), labelled as BLFO, BLFSO1, BLFSO2, BLFSO3 and BLSO for Se = 0%, 10%, 25%, 50%100% respectively were synthesized by sol–gel method. Nitrate salts of Bismuth and Lanthanum were stoichiometrically dissolved in acetic acid (5 ml) and ethylene glycol (5 ml) for 2 h. Iron nitrate and selenium powder (Se = 0%, 10%, 25%, 50%, 100%) were dissolved in acetic acid (10 ml) at 40 °C for 2 h using magnetic stirrer. Then, both the solutions were mixed for 3 h under constant magnetic stirring. The mixed solution was dried in oven at 90 °C for 12 h. The obtained gel was then calcined in the furnace at 600 °C for 3 h. After cooling, the calcined powder was ground to get the nanostructures. The flow chart representation of the synthesis procedure is shown below.

Table 1
Crystal structure Parameters obtained from the XRD patterns.

S·No	Sample	Average Crystallite Size (nm) [19]	Dislocation Density δ (10^{-16} lines/m^2) [19]	Microstrain [19]
1.	BLFO	26.10	0.0031	6.266
2.	BLFSO1	27.39	0.0026	5.501
3.	BLFSO2	35.45	0.0008	5.238
4.	BLFSO3	48.70	0.0004	2.814
5.	BLSO	34.96	0.0018	3.451

3. Results and discussions

3.1. X-ray diffraction

The XRD data were analysed to check the presence of various phases/impurities in the samples and to identify the crystal structure thereby helping in determining the structural and lattice parameters. The room temperature powder X-ray diffraction pattern of BLFO and the derived BLFSO nanomaterials calcined at 600 °C were recorded using the PANalytical X'Pert PRO powder X-ray Diffractometer system and the corresponding graphical plots of the samples are presented in Fig. 1. The BLFO sample revealed diffraction peaks (012) (210) (104) (110) (202) (024) (018) (214) showing a distorted perovskite based rhombohedral structure with R3c space group that is in agreement with the JCPDS card #01–086-1519. Abbasi et al., [11], have reported similar results with lanthanum doped BFO. On incorporating Se, the diffraction peak (012) became weak and the peak (210) intensified with increase in doping concentration. The sharp and high intensity peaks support the good crystallinity of as synthesized BFO nanostructures. The Fe peak (110) (202) were suppressed and completely disappeared in the BLSO sample due to the absence of Fe. Also, a slight shift in peaks toward the higher diffraction angles were observed on Se doping at peaks corresponding to (104) and (110) which could be ascribed to difference in ionic radius of dopants (Se = 0.64°A, La =1.032°A) than parent ions (Bi = 1.03°A), Fe (Fe = 0.78°A) [12–16]. A similar trend was previously reported for different rare-earth doped BFO nanoparticles [17]. Impurity phase of $Bi_{25.04}Fe_{0.84}O_{40}$ indexed between following (*hkl*) (2 0 4) and (101) indices (mentioned as * in Fig. 1) was noted in the BLFO sample which them disappeared on co-doping of Se.

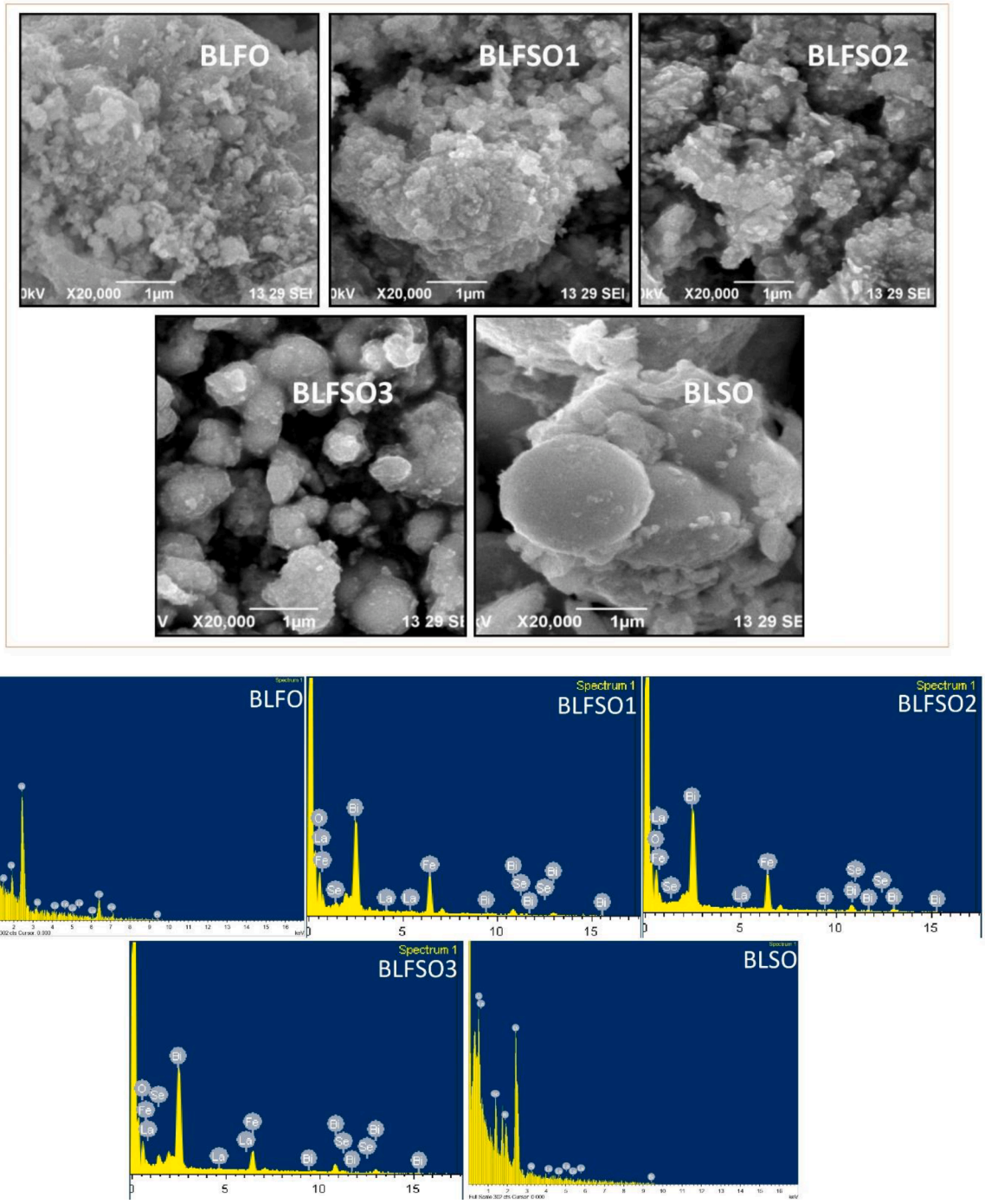

Fig. 2. (a). SEM micrographs of the prepared La, Se doped BFO nanostructures. (b). EDAX spectra of the prepared La, Se doped BFO nanostructures.

The crystallite size (D) calculated and tabulated using the Debye Scherer's formula was found to be increased with increase in doping concentration from 26 nm to 48 nm (Table 1). A Red shift of peaks are observed around 32° with an increase in Se concentration which indicated the increase in size of the doped samples. But for the BFSO sample, a shift toward the lower angle is noted, indicating a decrease in size. This change in size of the BLSO sample may be due to the absence of iron. The dislocation density of the doped samples was calculated and found to decrease with increase in doping concentration due to the increase in crystallite size of the doped samples. The decrease in dislocation density indicates that the nanostructures are more ordered and crystalline upon the incorporation of Se dopants. The lattice strain/ micro strain of the samples was also observed to decrease with increase in doping concentration. M. M. El-Okr et al. [18] have reported a decrease in microstrain values with increasing particle size due to the long annealing time in CoFe2O4 nanoparticles [18].

The incorporation of lanthanum (0.3 wt%) results in the phase transformation rhombohedral to orthorhombic [20,21]. Here, it is observed that the addition of Se with with Fe red shifts two theta in (104) (024) and (214) peaks that results in mixed phase of both rhombohedral and orthorhombic.

3.2. Scanning electron microscopy and EDAX

SEM analysis is useful in evaluating the change in morphology along with grain shape and size that is caused by the addition of dopants. Fig. 2

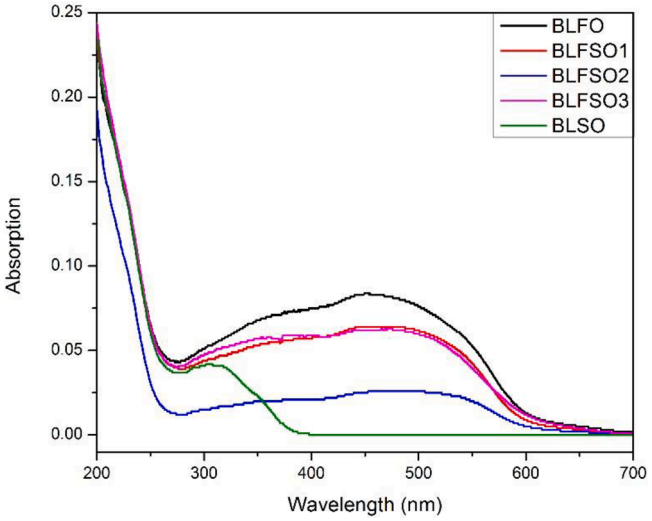

Fig. 3. UV–Vis absorption spectra of La, Se doped BFO nanostructures.

(a) shows the change in surface morphological features and shape of rare-Earth doped BFO nanstructures observed using Jeol JSM 6390 Scanning Electron Microscope. The BLSO nanoparticles showed smooth spheres and BLFO nanoparticles showed agglomerated flakes. The incorporation of Selenium in the BLFO samples (BLFSO) showed the transformation from agglomerated flakes to distinct flaky particles and then to spheres as the doping concentration increases. It is evident that the morphology of the samples were affected by the incorporation of selenium. Hence, the surface appears smoother with an increase in selenium concentration that can also be correlated to the decrease in the microstrain as observed from XRD. The change in the micro structures on La and Se substitution in BFO may enhance dielectric and magnetic properties that may impact energy storage properties of BLFSO nanostructures.

The compositional analysis was carried out for the $Bi_{0.92}La_{0.08}Fe_{1-x}Se_xO_3$ nanostructures to confirm the presence of rare earth dopants at the elemental level through Energy Dispersive X-ray spectroscopy (EDAX). The EDAX spectra of all the prepared samples as given in the figure below. It confirms the characteristic peaks for Bi, Fe, La and Se clearly. The absence of any other peaks indicates that the prepared La and Se doped BFO nanostructures have uniform dopant throughout the samples and that quality of all the prepared doped nanostructures are of single phase nature.

3.3. Optical analysis

The optical properties is related to the electronic structure and their band gaps. The UV–Vis absorption spectra was used to investigate the optical properties of rare-Earth (La, Se) doped BFO at room temperature in the wavelength range of 200 nm - 800 nm by using Shimadzu 2600 UV–Vis Spectrophotometer. A broad absorption spectra was observed for all the samples. The absorption peaks were observed at 613 nm (BLFO), 603 nm (BLFSO1), 609 nm (BLFSO2), 619 nm (BLFSO3), 390 nm (BLSO) (Fig. 3).

Incorporation of Se in BLFO results in red shifted absorption wavelengths but blue shifted on comparing with BLFO. Drastic change in absorption occurs in BLSO samples due to absence of Fe.

The optical absorption coefficient near the band edge follows the equation:

$$(\alpha h\nu)^n = A\left(h\nu - E_g\right)$$

where α, h, ν and E_g are absorption coefficient, Planck's constant, frequency of incident photons, and band gap, respectively, and A is a constant. The corresponding energy band gap of the material can be estimated using the Kubelka–Munk (K–M) theory, from the $(\alpha h\nu)^n$ vs. $h\nu$ plot by extrapolating the linear portion of the plot to zero. The bandgap calculations were done for the absorption wavelengths of each sample and the corresponding bandgap values were tabulated below.

Table 2
Calculated bandgap values of the prepared nanostructures.

Samples	BLFO	BLFSO1	BLFSO2	BLFSO3	BLSO
Bandgap	2.71 eV	2.68 eV	2.56 eV	2.55 eV	3.57 eV

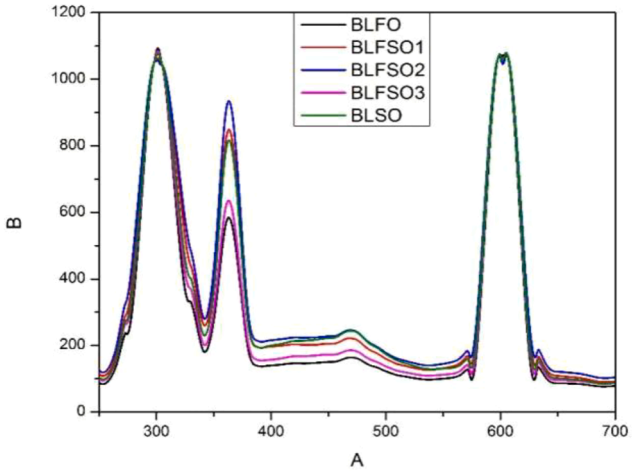

Fig. 4. PL spectra of La, Se doped BFO nanostructures.

The direct bandgap values of the samples were found to decrease with increase in doping concentration. For BLFO, the bandgap was found to be 2.71 eV which decreased to 2.67 ev in BLFSO samples (Table 2). For BFO samples, the reported direct bandgap values range upto 2.4 ev. The reported bandgap value for the bulk BFO is 3.00 ev [22]. Therefore, it is evient that the bandgap value has been reduced for the nanostructured doped BFO when compared to its bulk form. The optical bandgap of the prepared nanostructures were found to be decreasing with increasing dopant concentration which can be structural distortion found in the samples [23,24]. This reduction in the optical band gap perhaps may be due to the generation of new states within the band gap, which facilitates the motion of electrons from the valence bands to new produced local sates of the conduction band [25,26].

Photoluminescence spectroscopy (PL) is an effective method for investigating the presence of defects in semiconducting materials. Origin of defects in a synthesized sample depends on several factors such as: synthesis protocol, maintaining pH value during the synthesis, thermal treatment to the sample and type of dopants etc. [24]. Room temperature PL emission spectra were also investigated at the excitation wavelength 300 nm using Shimadzu RF-5301pc Spectrofluorophotometer. The PL spectra shows three emission peaks in the emission spectrum; one at 365 nm, and other two at 470 nm and 600 nm (Fig. 4). The characteristic peak at 365 nm is ascribed to the radiative emission of nanostructures during recombination of electron-hole pair while the other peaks are due to emission as a result of recombination owing to the defects and donor acceptor interaction [27]. Two additional kinks observed at 570 nm and 633 nm reveals strong emission in the visible region.

3.4. Dielectric analysis

The dielectric constant and dielectric loss of as-synthesized $Bi_{0.92}La_{0.08}Fe_{1-x}Se_xO_3$ samples were investigated in the frequency

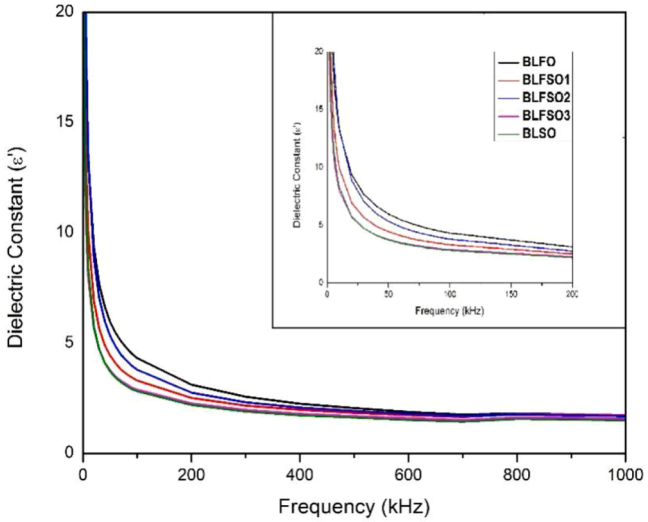

Fig. 5. Dielectric constant vs frequency plots of La, Se doped BFO nanostructures.

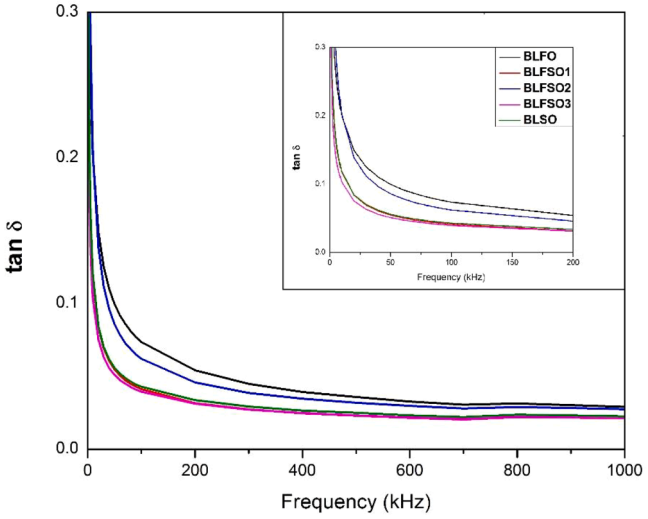

Fig. 6. Dielectric loss vs frequency plots of La, Se doped BFO nanostructures.

range 100 Hz to 1 MHz at room temperature using HIOKI Hi Tester LCR Meter, for evaluating dielectric performance. The dielectric properties of these nanostructures in this frequency range are rarely available because of persistence of leakage current [28]. The dielectric constant (ε') and tangent loss (tanδ) were plotted against frequency following the relations [29]:

$$\varepsilon' = \frac{C^{*}d}{\varepsilon o^{*}A}$$

Fig. 5 demonstrates increase in values of dielectric constant with increasing doping concentration and gradual decrease of dielectric constant with increasing frequency.

The energy dispersion indicated by the dielectric constant graph in Fig. 5 shows a decreasing trend with increasing frequency, which is a conventional ferrite behaviour. At low frequency, the dielectric constant depends upon different types of polarizations, i.e. interfacial, ionic, electronic, atomic polarization. But at high frequencies, only electronic polarization is responsible for the dielectric constant. So, there is a drastic decrease in dielectric constant values in the low frequency region, which later remains constant in the high frequency region. According to Kumar et al. [30] the rapid fall in dielectric constant at low frequency was due to inertia, which hinders the instantaneous polarization of the applied field. According to the Maxwell-Wagner two layer model, polarization is produced in any polycrystalline material due to well conducting grains separated by poor grain boundaries [30]. Hence, at lower frequencies, the space charges can follow the applied field due to their larger relaxation times, while at higher frequencies, they lag behind the applied field and hence, are unable to undergo relaxation [31]. The dielectric constant values were also found to decrease with increase in Se concentration. This variation of the dielectric constant points out the dispersion that occurred led by Maxwell interfacial polarization and has been in accord with the Koops phenomenological theory [29,32]. The dispersion of the dielectric constant may be caused by the hopping of electrons between La and Se ions. The large values of the dielectric constant in $Bi_{0.92}La_{0.08}Fe_{1-x}Se_xO_3$ can be understood as the replacement of Fe^{3+} ions by La^{2+} and Se^{2+}, which has been expected to introduce a higher density of vacancies and increase the probability of hopping conduction mechanism. The initial slow decrease in the dielectric constant has been consistent with the Koops model [32]. Moreover, nanocrystalline samples have high grain boundary density and so the nature of the grains and grain boundaries affects the electrical properties [33]. The in-homogeneity occurred because of grains and grain boundaries that lead to high dielectric values.

Fig. 6 shows the polarization lagging with respect to the alternating applied electric field, which is explained by the dielectric loss (tan δ). The main causes of dielectric loss are impurities and imperfections/deformities in the crystal lattice of dielectric materials. Similar to the dielectric constant graph, the dielectric loss also shows a decreasing pattern with increasing frequency and dopant concentration at the low frequency region and then remains constant at high frequencies. The decrease in loss tangent with increasing frequency may be attributed to the hopping frequency of the electron interchange between Fe^{3+} and Fe^{2+} ions at neighbouring octahedral sites [34]. The dielectric loss increases for all the samples with decreasing frequency without having any loss peak, which signifies that the synthesized material is homogeneous and stoichiometric with a uniform distribution of the grain/particles. The dielectric loss value is found to be highest for the BLFO sample that can be attributed to the presence of charge defects in the sample. The dielectric loss value is observed to be decreased with the addition of Se, which may be due to the decrease in charge defects that makes BLFSO nanostructures as potential candidates for energy storage applications.

It was also observed that both the dielectric constant and dielectric loss values were high initially, then they decreased drastically with increase in frequency in the low-frequency region and after a certain value at high frequency, it tends to remain constant. This phenomenon can be well described by the Maxwell-Wagner model, which is related to space charge relaxation [29].

3.5. Impedance analysis

Impedance spectroscopy is a powerful tool used to gain more information about the electrical heterogeneity and to distinguish the impedance contribution from grain, grain boundary and the electrode [35]. The variation of real part of impedance (Z') as a function of frequency at room temperature using HIOKI Hi Tester LCR Meter for $Bi_{0.92}La_{0.08}Fe_{1-x}Se_xO_3$ nanostructures are displayed.

The complex impedance can be denoted by

$$Z = Z' + iZ''$$

Where Z' and Z'' are the real and imaginary parts of the complex impedance.

$$Z' = \frac{Z}{d}cos\left[\varphi\left(\frac{3.14}{180}\right)\right]$$

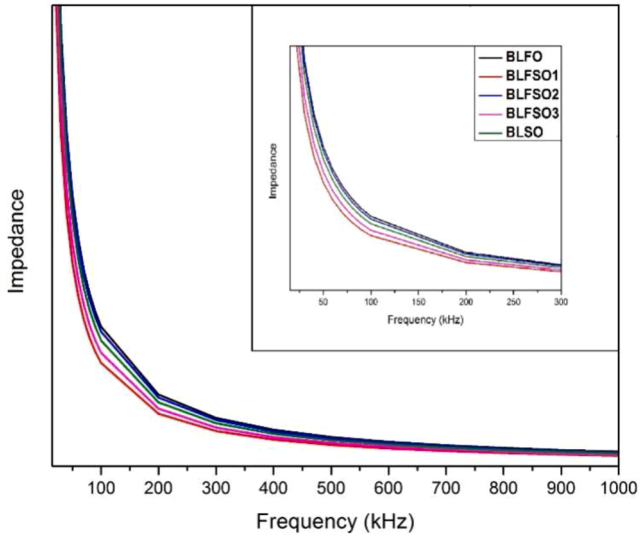

Fig. 7. Room temperature Impedance spectra for La, Se doped BFO nanostructures.

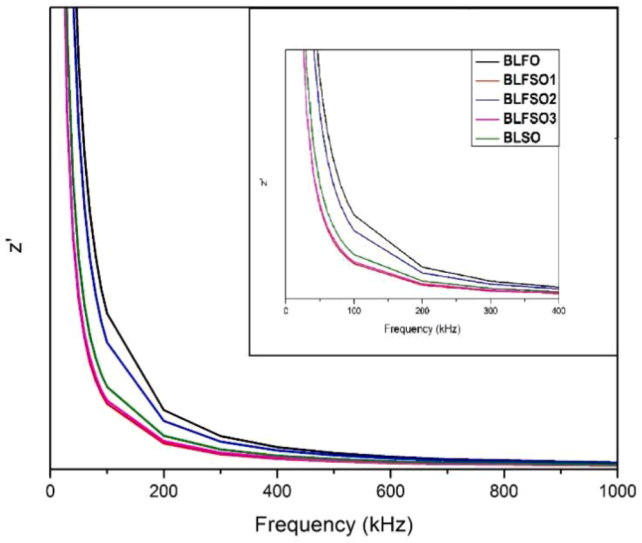

Fig. 8. Z' vs Frequency spectra of La, Se doped BFO nanostructures.

$$Z'' = \frac{Z}{d} sin\left[\varphi\left(\frac{3.14}{180}\right)\right]$$

Where Z is the complex impedance value measured from the HIOKI Hi Tester LCR Meter and d is the thickness of the pellet (0.002 m) and φ is the phase angle values obtained for the HIOKI Hi Tester LCR meter.

The complex impedance values of the BFO nanostructures at room temperature are plotted against the frequency (Fig. 7). It can be seen that the impedance values decrease rapidly at low frequencies and then continue to remain constant at high frequencies. To get a clear understanding of the impedance spectrum, the real and imaginary parts of the complex impedance were plotted against the frequency.

In Fig. 8, it can be seen that Z' decreased with increasing frequency, which might be ascribed to the improvement in the conduction mechanism. This enhancement in the conductive property of the nanostructures may be due to the electron hopping among the localized charge carriers, which are enriched with frequency of applied field [36]. At higher frequencies, the impedance values tend to be constant, which shows the frequency independent behaviour of Z'. This decreasing trend of impedance has been reported by Amin M et al., for La/Cr co-doping

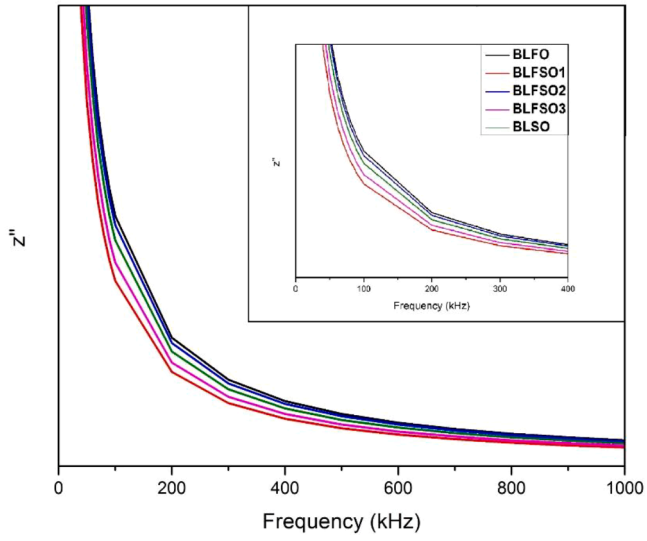

Fig. 9. Z'' vs Frequency spectra of La, Se doped BFO nanostructures.

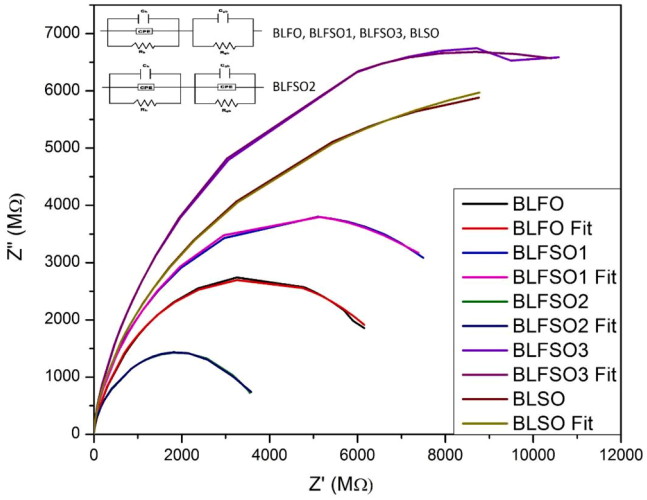

Fig. 10. Cole-Cole plot from impedance spectroscopy measurements.

[37] and Sr/Mn co-doping at Bi/Fe lattices in BFO [38]. Here, with the addition of Se, the Z' values were found to be decreased when compared to BLFO which represents the enhanced conduction of the nanostructures. But, the increase in Se concentration increased the impedance. As shown in the insets of Fig. 8 and Fig. 9. This increased resistivity may be due to the reduction in oxygen vacancies and the inhibition of fluctuation from the Fe^{3+} to Fe^{2+} state. Thus, the Se doping of the BLFO sample improved the insulating behaviour of the material, which is also responsible for improved magnetic properties. A similar decreasing trend was observed when the imaginary part of impedance (Z'') was plotted against frequency (Fig. 9).

Fig. 10 shows the Cole-Cole plots of La and Se doped BFO nanostructures. The appearance of a single semi-circle curve in BLFO, BLFSO1, BLFSO3 and BLSO curves represents a single Debye relaxation and explains the grain properties of the doped BFO sample. The semi-circle appears to be distorted appreciably at higher frequencies, thereby revealing deviation from the ideal Debye behaviour [39]. Obviously, the Z'' plot of the BFO sample exhibits only one semicircle with non-zero intercept on the Z' axis at high frequencies. The radius of curvature provides the resistivity of the sample, which is found to increase with the increase of Se doping concentration in BLFO samples. It is also noted that the BLFSO2 sample shows a depressed semi-circle

Table 3
Fitted values from the Zsimp software.

Compound Name	Rg	n	CPE	Cg	Rgb	n	CPE	Cgb
BLFO	5.69E12	2.54E-5	0.0004305	1.30E-5	5.9E9	_	_	6.7E-26
BLFSO1	1414	0.00038	3.24E-8	6.74E-5	7.78E9	_	_	8.31E-14
BLFSO2	2.78E9	1	6.82E-5	8.99E-8	6.39E9	0.3215	1.18E-11	6.07E-14
BLFSO3	2.89E4	2.23E-7	3.16E-8	0.0186	1.28E10	_	_	1.35E-24
BLSO	295.8	0.0014	6.82E-8	1.19E-5	1.043E10	_	_	6.83E-14

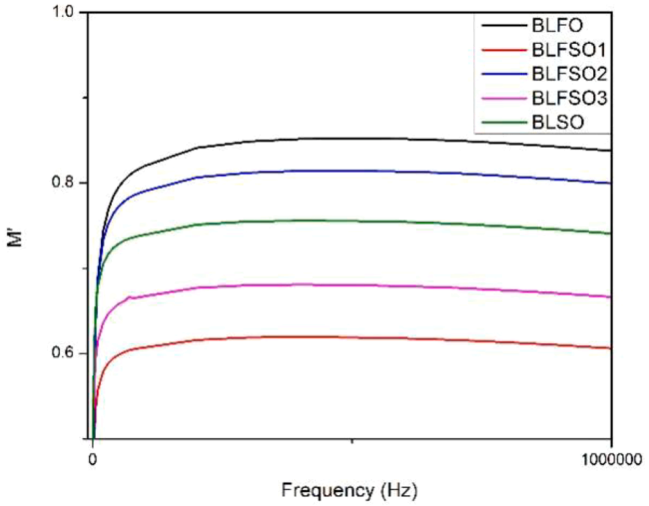

Fig. 11. M' vs Frequency spectrum of La, Se doped BFO nanostructures.

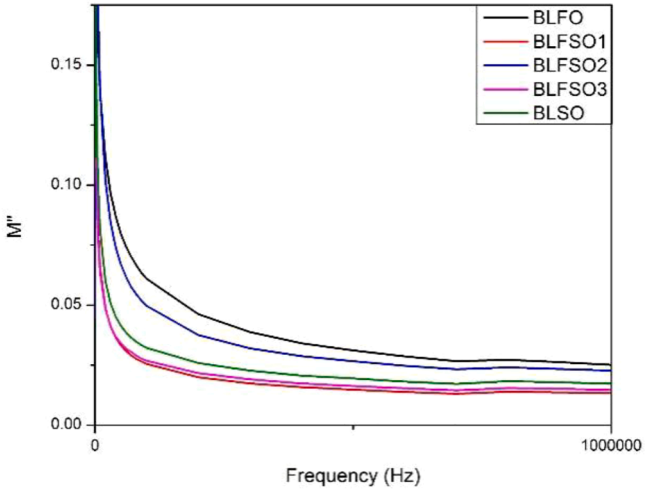

Fig. 12. M'' vs Frequency spectrum of La, Se doped BFO nanostructures.

compared to the other samples. The formation of depressed semi-circles may be due to inhomogeneity in size and distribution of grains in the ceramic sample [40]. To take account of this effect, one needs to introduce a constant-phase element (CPE) Q along with the elements R and C in the equivalent circuit for each of the contributions. All of the experimental data are fitted with equivalent electrical circuits by ZSIMPWIN software (Table 3).

3.6. Modulus analysis

Modulus analysis very much useful in studying the electrical characteristics of materials and to explore the conduction and relaxation phenomena involved within the dielectric materials. Normally, this

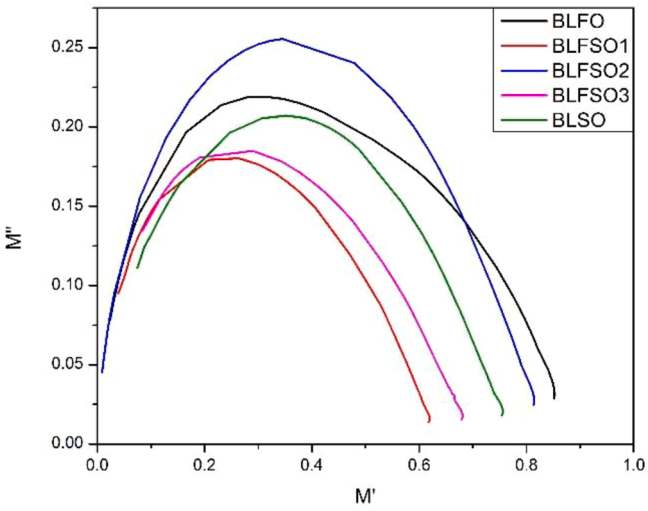

Fig. 13. Complex modulus plot of the prepared La, Se doped BFO nanostructures.

technique is used to inspect the hopping rate of charge careers, which contribute to the conduction process in dielectrics. The real (M') and imaginary (M'') parts of the complex electric modulus (M) was calculated using the relations [41]:

$$M' = \omega C_{\circ} Z''$$

$$M'' = \omega C_{\circ} Z'$$

Where $C_o = \varepsilon_o A/d$ (ε_o is permittivity of free space, A the area of the electrode surface and d the thickness of the sample).

Fig. 11 shows variation of M' over a wide frequency range at room temperature measurements. It is characterized by an increasing value of M' at the low frequency region followed by a saturated value in the high

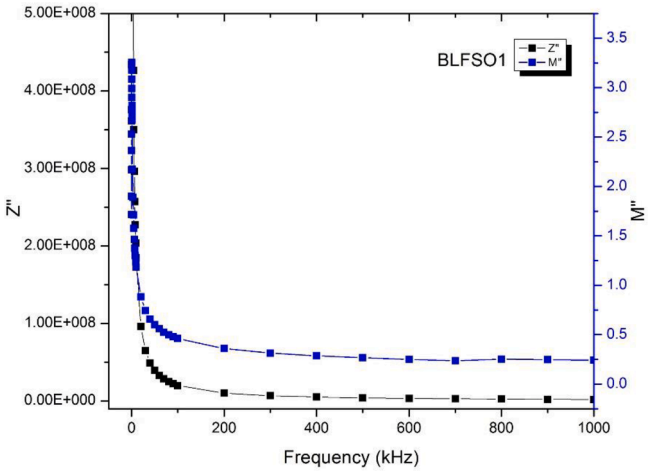

Fig. 14. Variation of Z'' and M'' of BLFSO1 with frequency.

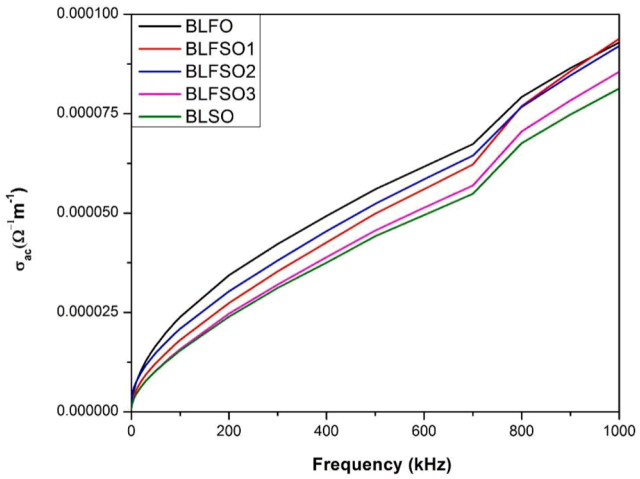

Fig. 15. Room temperature ac conductivity spectrum of La, Se doped BFO nanostructures.

frequency region. This increasing behaviour can be attributed to the short-range mobility of charge carriers [42]. On incorporation of Selenium to the BLFO nanostructures, value of M' decreased drastically almost nearing zero. But, with increase in the doping concentration of Selenium the value of M' increased.

Fig. 12 represents the variation of M" over a wide frequency range at room temperature measurements. It can be seen that the M" plot is similar to that of the Z". The imaginary component of the modulus has a direct dependence on the resistive part of impedance through the relation $M'' = \omega CoZ'$ [43].

Fig. 13 presents the complex modulus plots at room temperature for BLFSO nanostructures. Figure shows broad and asymmetric peaks indicating non - Debye relaxation i.e. the spreading of relaxation times with varying time constants. The Increase in Se doping concentrations increased the diameter of the arc.

To examine the short-range mobility of charge carriers, the imaginary components of impedance and modulus are plotted against frequency in Fig. 14. It has been reported that if the peaks of both the components Z′′ and M" occur at the same frequency, it is due to the long-range-type charge carriers [43,44]. If it does not occur, then it is due to short-range-type charge carriers [44].

3.7. Electrical conductivity analysis

For metal oxides, electrical conductivity can be determined from the dielectric and impedance measurements. The ac conductivity of the nanostructures can be calculated using the following relation [29]:

$$\sigma_{ac} = \varepsilon' \varepsilon_o \omega \tan\delta$$

here ε_o is permittivity of free space, ε' is the dielectric constant of the electrode material, tan δ is the tangent loss of the material and ω is the angular frequency equal to 2πf.

The frequency dependant ac conductivity spectrum of BLFSO system is illustrated in Fig. 15. From this spectrum, it is evident that all the doped samples exhibited very low ac conductivity depicting that high resistance from the impedance measurements. After a particularly high frequency, conductivity increased sharply. Such processes can be explained by Koop's model [45]. According to this model, poor conducting grain boundaries are responsible for low conductivity at lower frequencies, while The increase in σ_{ac} at high frequency is due to the hindrance posed by grain boundaries. The high frequency of the field promotes jumping of charge carriers between the localized states resulting improvement in conductivity [46].

3.8. Cyclic voltammetry

The cyclic voltammetry (CV) analysis of $Bi_{0.92}La_{0.08}Fe_{1-x}Se_xO_3$ samples for potential application in super capacitors was carried out using CH instrument- 600C. The three electrode system was used for the CV set-up. Super capacitive application also depends on nature of electrolyte 2 M NaOH was chosen as the electrolyte. Pt wire and Ag-Ag/Cl were used as the Counter electrode and reference electrode respectively. The working electrode was prepared by coating the active material (80%) + Carbon Black (10%) + PVDF (5%) with NMP on reused carbon cloth and dried in an oven overnight. The prepared electrodes

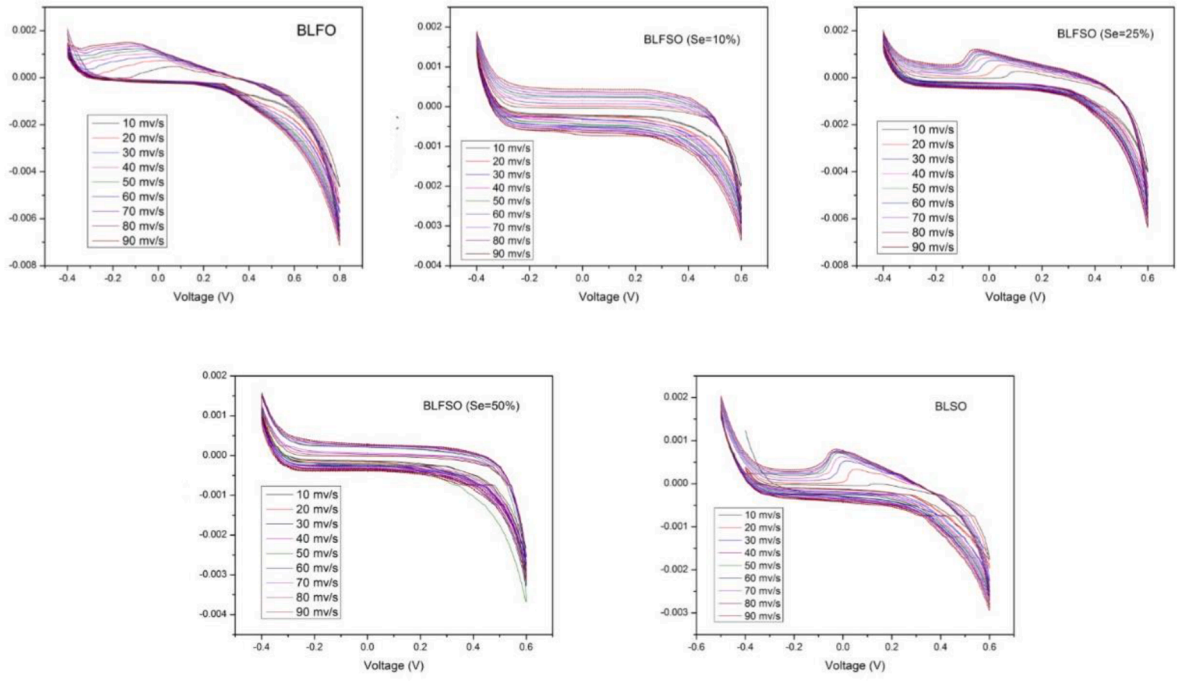

Fig. 16. Cyclic voltammetry graphs for La, Se doped BFO nanostructures using Carbon cloth sustrate.

Table 4
Specific capacitance values from cyclic voltammetry using reused carbon cloth as substrate.

Scan Rate	Specific Capacitance (F/g)				
	BLFO	BLFSO1	BLFSO2	BLFSO3	BLSO
10 mV/s	20.678	12.808	6.756	3.398	3.2
20 mV/s	19.438	8.092	4.88	2.526	1.758
30 mV/s	6.246	6.658	3.92	2.00	1.592
40 mV/s	4.822	6.406	3.38	1.83	1.478
50 mV/s	5.54	6.552	3.068	2.146	1.354
60 mV/s	7.188	6.122	2.856	1.7024	1.262
70 mV/s	5.518	6.046	2.66	1.57	1.202
80 mV/s	6.46	5.93	2.534	1.524	1.156
90 mV/s	6.3	5.96	2.426	1.494	1.114

were subjected to different voltage scan rates from 10 mVs^{-1} to 90 mVs^{-1} in the potential window of −0.35 to 0.6 V (Fig. 16).

The specific capacitance of La doped BFO is very less reported, whereas, for Selenium doped BFO and La, Se co-doped BFO, has not yet been reported elsewhere. The specific capacitance of the electrodes were calculated form cyclic voltammetry using the following relation [47]:

$$C = \frac{\int I.dV}{mk(V_2 - V_1)}$$

Where, ∫I.dv represents the integration of the voltammetric curve, m is the mass of the active material, k is the scan rate and (V_2-V_1) is the potential window. Moreover, for these electrodes, the increase of current response with increasing scan rate was observed, that might by due to effect of scan rate on the migration of electrolytic ions and their diffusion into the electrode. At a relatively lower scan rate, a thick diffusion layer grows on the surface of the electrode, and limits the flux of electrolytic ions toward the electrode. This factor results in lower current, whereas, at a higher scan rate, the diffusion layer cannot grow on the electrode surface. Therefore, the enhanced electrolyte flex toward the electrodes leads to an increase of current [39].

In CV curve, with an increase of scanning rate the shifting of both the upper and lower peaks toward positive and negative directions respectively was observed. This might be because of development of over potential, which limits the faradic reactions [39].

A maximum capacitance of 20 F/g was observed at 10 mV/s for La doped BFO coated on the reused carbon cloth substrate, which is very less than the previous reported results of La doped BFO (Table 4). With an aim to improve the specific capacitance, the cyclic voltammetry was repeated for the same samples using Nickel foam as the substrate to study the effect of substrate in the specific capacitance values. The three electrode system was used for the CV set-up and the cyclic voltammetry analysis was carried out using the same electrolyte, 2 M NaOH. The working electrode was prepared by coating the active material (80%) + Carbon Black (10%) + PVDF (5%) with NMP on Nickel foam and dried for a few minutes. The prepared electrodes were subjected to different voltage scan rates from 10 mVs^{-1} to 90 mVs^{-1} in the potential window of −0.1 to 0.5 (Fig. 17). Here, the maximum capacitance observed for La doped BFO was 36 F/g (Table 5).

3.9. Magnetic analysis

The room temperature magnetic hysteresis (M-H) loops showing the variation of magnetization with respect to the applied field at room temperature is shown in Fig. 18. It was observed that La, Se doped BFO nanoparticles exhibit a weak ferromagnetism (4.27 emu/g) with saturation magnetization and a non-zero remanent magnetization (M_r =

Table 5
Specific capacitance values from cyclic voltammetry using nickel foam as substrate.

Scan Rate	Specific Capacitance (F/g)				
	BLFO	BLFSO1	BLFSO2	BLFSO3	BLSO
10 mV/s	36.22	21.48	10.76	7.72	4.38
20 mV/s	32.63	25.90	12.37	8.53	6.56
30 mV/s	29.05	24.98	12.73	8.85	6.96
40 mV/s	26.95	19.25	10.24	7.08	5.58
50 mV/s	25.31	22.42	13.55	9.10	7.18
60 mV/s	24.06	21.52	13.83	9.10	7.25
70 mV/s	23.18	20.80	13.90	9.07	7.26
80 mV/s	22.37	20.17	13.86	9.05	7.27
90 mV/s	21.73	19.67	13.89	9.07	7.28

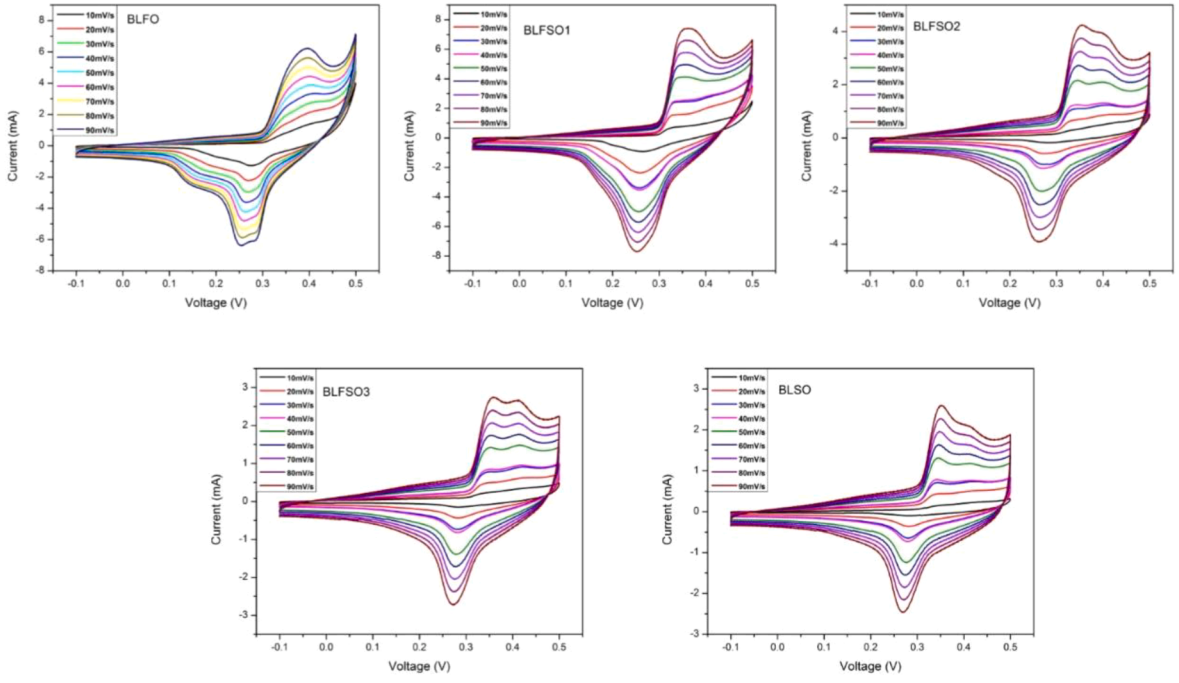

Fig. 17. Cyclic voltammetry graphs for La, Se doped BFO nanostructures using Ni foam substrate.

Table 6
Magnetic parameters obtained from the M-H loops.

Samples	BLFO	BLFSO1	BLFSO2	BLFSO3	BLSO
M_s (emu/g)	4.565	2.704	3.266	3.11	0
M_r (emu/g)	1.564	1.124	1.399	1.18	0
H_c (Oe)	0.4	2	13	23	0

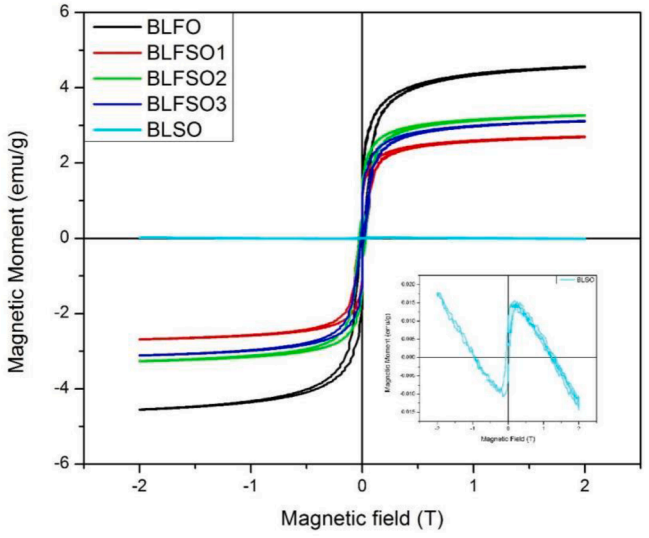

Fig. 18. Room temperature M-H loops of La, Se doped BFO nanostructures.

1.564 emu/g). The behaviour of the high field linear M–H curve is commonly observed in bulk $BiFeO_3$ due to the antiferromagnetic arrangement of Fe^{3+} spins [48]. Hence, the weak ferromagnetic behaviour is due to the destruction of the spiral magnetic ordering [49]. Dopants play a major role in altering the magnetization because of the varied ionic radii of La^{3+}, Bi^{3+} and Se^{4+} ions or due the magneto electric coupling. On the other hand, the $Bi_{0.92}La_{0.08}Fe_{1-x}Se_xO_3$ compounds showed a ferromagnetism enhancement of upto 3.26 emu/g (Table 6). The origin of weak ferromagnetism in the nanoparticles is possibly due to the canting of the spins mainly because of the fact that when particle size decreases, number of surface asymmetry atoms increases. Due to this, the angle of the helical ordered spin arrangement is changed and hence the net magnetic moment appears [50].

In addition to this, they also showed a small coercive field. The increased coercivity with increased doping concentration can also be related to the structural and morphological changes of the nanoparticles [51]. When selenium doping concentration becomes maximum, the ferromagnetic nature is changed to diamagnetic due to the absence of iron. It is regarded that these enhanced magnetic properties of Se doped BLFO nanostructures will enable them to have great practical applications in magnetic data storage devices.

4. Summary and conclusions

In this study, the structure, morphology, optical dielectric and magnetic properties of La and Se co-doped BFO synthesized via the solvothermal method were systematically analysed. The composition of the samples were varied as $Bi_{0.92}La_{0.08}Fe_{1-x}Se_xO_3$, (x = 0%, 10%, 25%, 50%, 100%). Structural and morphological investigations were done using XRD and SEM. The optical analysis showed a wide absorption spectra with reduced bandgap when compared to bulk BFO. Enhanced magnetic properties enabled these nanostructures as magnetic data storage devices. The dielectric constant and dielectric loss values were found to be decreased with increase in frequency that made the La, Se co-doped BFO nanostructures a potential candidate for energy storage applications. The specific capacitance was analysed using cyclic voltammetry for all the prepared samples and the maximum Specific capacitance of 36.2 F/g at 10 mV/s scan rate was observed for BLFO sample and 21.48 F/g was observed for BLFSO1 (x = 10%) which then decreased on further doping. But weak ferromagnetic properties of these materials holds hope to find applications in magnetic energy storage devices. Selenium doped samples were not much reported for energy storage applications. This present work outlines its performance in energy storage applications.

Declaration of Competing Interest

The authors declare that they have no known competing financial interests or personal relationships that could have appeared to influence the work reported in this paper.

Data availability

Data will be made available on request.

References

[1] X. Yang, Z. Zhou, T. Nan, Y. Gao, G.M. Yang, M. Liu, N.X. Sun, Recent advances in multiferroic oxide heterostructures and devices, J. Mater. Chem. C 4 (2016) 234–243, https://doi.org/10.1039/c5tc03008k.
[2] C. Lu, W. Hu, Y. Tian, T. Wu, Multiferroic oxide thin films and heterostructures, Appl. Phys. Rev. 2 (2015), 021304, https://doi.org/10.1063/1.4921545.
[3] Jahangeer Ahmed, Manawwer Alam, M.A. Majeed Khan, Saad M. Alshehri, Bifunctional electro-catalytic performances of NiMoO4-NRs@RGO nanocomposites for oxygen evolution and oxygen reduction reactions, J. King Saud Univ. Sci. (2021), https://doi.org/10.1016/j.jksus.2020.101317.
[4] Hongbo Ding, Jiang Zhou, Apparao Rao, Bingan Lu, Cell-like-carbon-micro-spheres for robust potassium anode, Natl. Sci. Rev. nwaa276 (2020), https://doi.org/10.1093/nsr/nwaa276.
[5] Lutong Shan, Yiren Wang, Shuquan Liang, Boya Tang, Yongqiang Yang, Ziqing Wang, Lu Bingan, Jiang Zhou, Interfacial adsorption–insertion mechanism induced byphase boundary toward better aqueous Zn-ion battery, InfoMat 3 (2021) 1028–1036, https://doi.org/10.1002/inf2.12223.
[6] Ji-Chi Liu, Zi-Hang Huang, Tian-Yi Ma, Aqueous Supercapacitor with ultrahigh voltage WindowBeyond 2.0 volt, Small Struct. 1 (2020), https://doi.org/10.1002/sstr.202000020, 2000020.
[7] Yonggang Wang, Yongyao Xia, Recent Progress in Supercapacitors: from materials design to system construction, Adv. Mater. 25 (37) (2013) 5336–5342, https://doi.org/10.1002/adma.201301932.
[8] Xin Gao, Hengwei Zhang, Erjun Guo, Fei Yao, Zengze Wang, Hongyan Yue, Hybrid two-dimensional nickel oxide-reduced graphene oxide nanosheets for supercapacitor electrodes, Microchem. J. (2021), https://doi.org/10.1016/j.microc.2021.105979.
[9] M. Jayachandran, Aleena Rose, T. Maiyalagan, N. Poongodi, T. Vijayakumar, Effect of various aqueous electrolytes on the electrochemical performance of V2O5 spindle-like nanostructures as electrode material for supercapacitor application, J. Mater. Sci. Mater. Electron. (2021), https://doi.org/10.1007/s10854-021-05378-8.
[10] A. Joana Preethi, M. Ragam, Effect of doping in multiferroic BFO: a review, J. Adv. Dielectr. 11 (6) (2021), https://doi.org/10.1142/S2010135X21300012, 2130001.
[11] Muhammad Ali Abbasi, Zeeshan Ali, Zahid Qamar, Khurram Shahzad, Humera Khatoon Siddiqui, Muhammad Atif, Zulqurnain Ali, Waqas Khalid, Phase pure synthesis of lanthanum doped bismuth ferrite nanostructures for the adsorption of doxorubicin, Ceram. Int. (2021), https://doi.org/10.1016/j.ceramint.2021.02.018.
[12] Y.Y. Gurkan, E. Kasapbasi, Z. Cinar, Enhanced solar photocatalytic activity of TiO2 by selenium (IV) ion-doping: characterization and DFT modeling of the surface, Chem. Eng. J. 214 (2013) 34–44.
[13] P. Tang, D. Kuang, S. Yang, Y. Zhang, The structural, optical and enhanced magnetic properties of Bi1-xGdxFe1-yMnyO3 nanoparticles synthesized by sol-gel, J. Alloys Compd. 622 (2015) 194–199.
[14] R. Palai, R.S. Katiyar, H. Schmid, P. Tissot, S.J. Clark, J. Robertson, S.A.T. Redfern, G. Catalan, J.F. Scott, Bphase and g-b metal-insulator transition in multiferroic BiFeO3, Phys. Rev. B: Condens. Matter Mater. Phys. 77 (2008) 014110–014121.
[15] G. Singh, L.N.K. Verma, Magnetoelectric coupling in multiferroic Tb-doped BiFeO3 nanoparticles, Mater. Lett. 111 (2013) 55–58.
[16] Y.B. Yao, C.L. Mak, Optical, ferroelectric and magnetic properties of multiferroelectric BiFeO3–(K0.5Na0.5)0.4 (Sr0.6Ba0.4)0.8Nb2O6 thin lms, J. Alloys Compd. 586 (2014) 448–455.
[17] Z. Hu, D. Chen, S. Wang, N. Zhang, L. Qin, Y. Huang, Facile synthesis of Sm-doped BiFeO3 nanoparticles for enhanced visible light photocatalytic performance, Mater. Sci. Eng. B 220 (2017) 1–12.
[18] M.M. El-Okr, M.A. Salem, M.S. Salim, R.M. El-Okr, M. Ashoush, H.M. Talaat, J. Magn. Magn. Mater. 323 (2011) 920–926.

[19] Ritesh Verma, Ankush Chauhan, Neha, Khalid Mujasam Batoo, Rajesh Kumar, Muhammad Hadhi, Emad H. Raslan, Effect of calcination temperature on structural and morphological properties of bismuth ferrite nanoparticles, Ceram. Int. (2020), https://doi.org/10.1016/j.ceramint.2020.09.220. S0272884220329370.
[20] Z.V. Gabbasova, M.D. Kuz'min, A.K. Zvezdin, I.S. Dubenko, V.A. Murashov, D. N. Rakov, I.B. Krynetsky, Bi1−xRxFeO3 (R=rare earth): a family of novel magnetoelectrics 158(9), 1991, pp. 491–498, https://doi.org/10.1016/0375-9601(91)90467-m.
[21] A.V. Zalesskii, A.A. Frolov, T.A. Khimich, A.A. Bush, Composition-induced transition of spin-modulated structure into a uniform antiferromagnetic state in a Bi1−xLaxFeO3system studied using57Fe, NMR. 45 (1) (2003) 141–145, https://doi.org/10.1134/1.1537425.
[22] Reda Moubah, Guy Schmerber, Olivier Rousseau, Dorothée Colson, Michel Viret, Photoluminescence investigation of defects and optical band gap in multiferroic BiFeO$_{3}$ single crystals, Appl. Phys. Express 5 (3) (2012) 035802, https://doi.org/10.1143/APEX.5.035802.
[23] Vimala Dhayal, S.Z. Hashmi, Upendra Kumar, B.L. Choudhary, A.E. Kuznetsov, Saurabh Dalela, Shalendra Kumar, Savas Kaya, S.N. Dolia, P.A. Alvi, Spectroscopic studies, molecular structure optimization and investigation of structural and electrical properties of novel and biodegradable chitosan-GO polymer nanocomposites, J. Mater. Sci. (2020), https://doi.org/10.1007/s10853-020-05093-5.
[24] Khushboo Punia, Ganesh Lal, Saurabh Dalela, Satya Narain Dolia, Parvez Ahmad Alvi, Shiv K. Barbar, Kunal B. Modi, Sudhish Kumar, A comprehensive study on the impact of Gd substitution on structural, optical and magnetic properties of ZnO nanocrystals, J. Alloys Compd. (2021), https://doi.org/10.1016/j.jallcom.2021.159142.
[25] Kamal Kumar Khichar, Suraj Bhan Dangi, Vimala Dhayal, Upendra Kumar, Sonia Zeba Hashmi, Veera Sadhu, Banwari Lal Choudhary, Shalendra Kumar, SavaÅ Kaya, Aleksey E. Kuznetsov, Saurabh Dalela, Saral K. Gupta, Parvez Ahmad Alvi, Structural, optical, and surface morphological studies of ethyl cellulose/graphene oxide nanocomposites, Polym. Compos. (2020), https://doi.org/10.1002/pc.25576.
[26] Shalendra Kumar, Mayuri Sharma, Rezq Naji Aljawfi, K.H. Chae, Rajesh Kumar, Sourabh Dalela, Adil Alshoaibi, Faheem Ahmed, P.A. Alvi, Tailoring the structural, electronic structure and optical properties of Fe: SnO2 nanoparticles, J. Electron Spectrosc. Relat. Phenom. 240 (2020) 146934, https://doi.org/10.1016/j.elspec.2020.146934.
[27] Yongping Li, Yongcheng Zhang, Wanneng Ye, Jianqiang Yu, Chaojing Lu, Linhua Xia, Photo-to-current response of Bi2Fe4O9 nanocrystals synthesized through a chemical co-precipitation process, New J. Chem. 36 (6) (2012) 1297, https://doi.org/10.1039/C2NJ40039A.
[28] A. Srivastava, A.K. Singh, O.N. Srivastava, H.S. Tewari, K.B. Masood, J. Singh, Magnetic and dielectric properties of La and Ni co-substituted BiFeO3 nanoceramics, Front. Phys. 8 (2020), https://doi.org/10.3389/fphy.2020.00282.
[29] Naima Zarrin, Shahid Husain, Wasi Khan, Samiya Manzoor, Sol-gel derived cobalt doped LaCrO3: structure and physical properties, J. Alloys Compd. 784 (2019) 541–555, https://doi.org/10.1016/j.jallcom.2019.01.018.
[30] A. Kumar, P. Sharma, W. Yang, J. Shen, D. Varshney, Q. Li, Effect of La and Ni substitution on structure, dielectric and ferroelectric properties of BiFeO3 ceramics, Ceram. Int. 42 (2016) 14805e12.
[31] O. Singh, A. Agarwal, S. Sanghi, A. Das, Investigation of crystal structure, dielectric and magnetic properties in La and Nd co-doped BiFeO3 multiferroics, J. Magn. Magn. Mater. 426 (2017) 369e74.
[32] C.G. Koops, On the dispersion of resistivity and dielectric constant of some semiconductors at audiofrequencies, Phys. Rev. 83 (1951) 121–125, https://doi.org/10.1103/PhysRev.83.121.
[33] A.M. Larson, P. Moetakef, K. Gaskell, C.M. Brown, G. King, E.E. Rodriguez, Inducing ferrimagnetism in insulating hollandite Ba1.2Mn8O16, Chem. Mater. 27 (2015) 515–525, https://doi.org/10.1021/cm503801j.
[34] D. Ravinder, K. Vijaya Kumar, Dielectric behaviour of erbium substituted Mn-Zn ferrites, Bull. Mater. Sci. 24 (2001) 505–509.
[35] J.T.S. Irvine, D.C. Sinclair, A.R. West, Electroceramics: characterization by impedance spectroscopy, Adv. Mater. 2 (3) (1990) 132–138, https://doi.org/10.1002/adma.19900020304.
[36] Khalid Mujasam Batoo, Feroz Ahmed Mir, M.-S. Abd El-sadek, M. Shahabuddin, Niyaz Ahmed, Extraordinary high dielectric constant, electrical and magnetic properties of ferrite nanoparticles at room temperature, J. Nanopart. Res. 15 (11) (2013) 2067, https://doi.org/10.1007/s11051-013-2067-6.
[37] Muhammad Amin, Hafiz Muhammad Rafique, Ghulam M. Mustafa, Asif Mahmood, Shahid M. Ramay, Shahid Atiq, S.M. Ali, Effect of La/Cr co-doping on dielectric dispersion of phase pure BiFeO3 nanoparticles for high frequency applications, J. Mater. Res. Technol. (2021), https://doi.org/10.1016/j.jmrt.2021.05.066.
[38] M. Amin, H.M. Rafique, M. Yousaf, S.M. Ramay, S. Atiq, Structural and impedance spectroscopic analysis of Sr/Mn modified BiFeO3 multiferroics, J. Mater. Sci. Mater. Electron. 27 (2016) 11003e11.
[39] Mahebub Alam, Keshab Karmakar, Monalisa Pal, Kalyan Mandal, Electrochemical Supercapacitor based on double perovskite Y2NiMnO6 nanowires, RSC Adv. (2016), https://doi.org/10.1039/C6RA23318J.
[40] V. Purohit, R. Padhee, R.N.P. Choudhary, Structural and electrical properties of Bi(Mg0.5Ti0.5)O3 ceramic, J. Mater. Sci. Mater. Electron. 29 (2018) 5224–5232.
[41] A.K. Jha Priyanka, Electrical characterization of zirconium substituted barium titanate using complex impedance spectroscopy, Bull. Mater. Sci. 36 (1) (2013) 135–141, https://doi.org/10.1007/s12034-013-0420-0.
[42] G.M. Mustafa, S. Atiq, S.K. Abbas, S. Riaz, S. Naseem, Tunable structural and electrical impedance properties of pyrochlores based Nd doped lanthanum zirconate nanoparticles for capacitive applications, Ceram. Int. 44 (2018) 2170e7.
[43] Prabhasini Gupta, P.K. Mahapatra, R.N.P. Choudhary, Structural, dielectric, impedance, and modulus spectroscopy of BaSnO3-modified BiFeO3, J. Phys. Chem. Solids (2019) 109217, https://doi.org/10.1016/j.jpcs.2019.109217.
[44] N. Kumar, S.K. Patri, R.N.P. Choudhary, Frequency-temperature response of a new multiferroic, J. Alloys Compd. 615 (2014) 456, https://doi.org/10.2298/PAC1403121K.
[45] Ompal Singh, Ashish Agarwal, Sujata Sanghi, Amitabh Das, Anju, Investigation of crystal structure, dielectric and magnetic properties in La and Nd co-doped BiFeO3 multiferroics, J. Magn. Magn. Mater. (2016), https://doi.org/10.1016/j.jmmm.2016.11.109. S030488531630806X.
[46] Jayant Kolte, Paresh H. Salame, A.S. Daryapurkar, P. Gopalan, Impedance and AC conductivity study of nano crystalline, fine grained multiferroic bismuth ferrite ($BiFeO_3$), synthesized by microwave sintering, AIP Adv. 5 (9) (2015), 097164, https://doi.org/10.1063/1.4931818.
[47] Muhammad Faisal Iqbal, Mahmood Ul Hassan, Aamir Razaq, Muhammad Naeem Ashiq, Farhat Yasmeen, Khurrum Saleem Joya, Shafqat Abbass, Valentino Kaneti, Yusuf, Alowasheeir Azhar, Azhar, Excellent effect of graphene oxide thin film on growth and electrochemical performance of hierarchical zinc Sulfide Nanoweb for Supercapacitor applications, ChemElectroChem. (2018), https://doi.org/10.1002/celc.201800633.
[48] S.R. Das, R.N.P. Choudhary, P. Bhattacharya, R.S. Katiyar, P. Dutta, A. Manivannan, M.S. Seehra, Structural and multiferroic properties of La-modified BiFeO3 ceramics 101(3), 2007, https://doi.org/10.1063/1.2432869, 34104–0.
[49] G.S. Arya, R.K. Sharma, N.S. Negi, Enhanced magnetic properties of Sm and Mn co-doped BiFeO3 nanoparticles at room temperature, Mater. Lett. 93 (2013) 341–344, https://doi.org/10.1016/j.matlet.2012.11.131.
[50] Claude Ederer, Nicola A. Spaldin, Weak ferromagnetism and magnetoelectric coupling in bismuth ferrite, Phys. Rev. B 71 (6) (2005) 060401, https://doi.org/10.1103/PhysRevB.71.060401.
[51] Haiyang Dai, Zhenping Chen, Tao Li, Yong Li, Microstructure and properties of Sm-substituted BiFeO3 ceramics, J. Rare Earths 30 (11) (2012) 1123–1128, https://doi.org/10.1016/s1002-0721(12)60191-4.